Acta Materialia 234 (2022) 117956

Contents lists available at ScienceDirect

Acta Materialia

journal homepage: www.elsevier.com/locate/actamat

Full length article

Multimodal assessment of mechanically induced transformation in metastable multi-phase steel using X-ray nano-tomography and pencil-beam diffraction tomography

Hiroyuki Toda[a,*], Kyosuke Hirayama[b], Kai Okamura[a], Takafumi Suzuki[a], Akihisa Takeuchi[c], Masayuki Uesugi[c], Hiro Fujihara[a]

[a] Department of Mechanical Engineering, Kyushu University, 744, Motooka, Nishi ward, Fukuoka city, FUKUOKA 819-0395, Japan
[b] Department of Materials Science and Engineering, Kyoto University, Yoshida Honmachi, Sakyo-ku, KYOTO 606-8501, Japan
[c] Japan Synchrotron Radiation Research Institute, 1-1-1, Kouto, Sayo-cho, Sayo-gun, HYOGO 679-5198, Japan

ARTICLE INFO

Article history:
Received 24 November 2021
Revised 11 April 2022
Accepted 14 April 2022
Available online 17 April 2022

Keywords:
Mechanically induced transformation
C-Mn-Si steel
Nano-tomography
X-ray diffraction
Mechanical driving force

ABSTRACT

A combination of X-ray nano-tomography and pencil-beam diffraction tomography was utilized for multimodal assessment of the mechanically induced transformation of individual retained austenite grains during tensile deformation in a 0.1C-5Mn-1Si multi-phase steel. In the present study, a newly developed high energy (20 - 30 keV) and high resolution (spatial resolution of 0.16 μm in this study) X-ray nano-tomography technique was applied for the first time to the in-situ observation of a steel under external loading. The gradual transformation, plastic deformation, and rotation behaviour of the individual austenite grains were clearly observed in 3D. It was revealed that the early stage of the transformation was dominated by the stress-assisted transformation that can be associated with measured mechanical driving force, whilst the overall transformation was dominated by the strain-induced transformation that is interrelated with measured dislocation multiplication. The transformation behaviour of individual grains was classified according to their initial crystallographic orientation and size. Noteworthy was the high stability of coarse austenite grains (i.e., 2.5 μm or larger in diameter), contrary to past reports in the literature. Characteristic rotation behaviour and wide data dispersion were also observed in the case of the individual austenite grains. It was conclusively demonstrated that such characteristic behaviour partly originated from interactions with surrounding soft and hard phases. The origins of these characteristics are discussed by combining the image-based and diffraction-based information.

1. Introduction

There has been growing interest in dual-phase, austenite/ferrite steels [1–3]. Of these, C-Mn-Si multi-phase steels with meta-stable retained austenite have attracted much research attention. The retained austenite phase, which is embedded as a minor phase in a ferrite-based microstructure, is stable at room temperature due to the carbon enrichment of austenite that takes place during thermo-mechanical processes [4–6]. The retained austenite phase transforms into martensite with volume expansion under external loading, which increases the work hardening rate of a steel, thereby delaying the onset of necking. This has a beneficial effect on the strength-ductility balance of multi-phase steels. Manganese also segregates into austenite, resulting in increased stability [5–8], while silicon suppresses carbide formation and thereby optimizes austenite stability [9].

The beneficial effect of the austenite-to-martensite transformation is obtainable only when the transformation occurs at an optimum applied strain during loading [10]. It is reported that the increase in the volume fraction of retained austenite sometimes results in low stability under loading due to reduced average carbon content [11]. It is therefore of crucial importance to control the stability of retained austenite in C-Mn-Si multi-phase steels, by optimizing the volume fraction of this phase.

It has been well documented that the stability of retained austenite depends on various factors besides the abovementioned chemical composition. Microstructural features, such as the morphology, size, and spatial distribution of the retained austenite,

* Corresponding author: Kyosuke Hirayama, Kyoto University Yoshida Campus: Kyoto Daigaku, Japan.
E-mail address: toda@mech.kyushu-u.ac.jp (H. Toda).

https://doi.org/10.1016/j.actamat.2022.117956

along with the influence of surrounding phases, are the most important factors, as well as mechanical conditions such as the strain rate and stress state [12,13]. amongst the relevant studies, Samek et al. demonstrated that the M_s^{σ} temperature (i.e., the austenite-to-martensite transformation temperature at which the stress reaches the yield stress of retained austenite) decreased rapidly with a decrease in the average retained austenite particle size in a C-1.5Mn-1.5Si steel, becoming 10 °C for a carbon content of 1.2 - 1.4% and average particle diameter of 1.0 - 1.2 μm [14]. Cai et al. estimated the optimum retained austenite particle size to be 0.6 μm for 0.18C-11Mn-3.8Al steel, by considering the elastic strain energy and work hardening behaviour [15]. Haidemenopoulos et al. designed a model based on the nucleation site potency distribution, and demonstrated that refinement of the austenite particle size is effective for stabilizing austenite, by suppressing the strain-induced transformation kinetics [16]. The influence of the phases that surround retained austenite has also been well investigated. amongst the study results, retained austenite was more stable when surrounded by bainitic ferrite than by ferrite [17,18], and retained austenite grains embedded in a larger ferrite grain were more stable than those at grain boundaries between ferrite grains [19]. The effects caused by surrounding phases are attributed to the carbon concentration (e.g., retained austenite adjacent to bainitic ferrite has a higher carbon content [18]), and stress/strain partitioning and localization due to strength differences [14,18]. It has been clearly demonstrated in ref. [6] that there is some variability in the final carbon enrichment between different retained austenite islands [6]. In terms of retained austenite morphology, Chiang et al. experimentally compared lamellar and equiaxed austenite [20], and found that the former was more stable due to its surrounding microstructure (i.e., bainitic ferrite), its higher carbon content due to the difference in volume fraction, and its greater size. The stability difference due to retained austenite morphology was therefore attributable to the aforementioned factors.

In retained austenite bearing steels, traditional metallographic preparation, such as mechanical cutting and polishing, inevitably introduces superficial austenite-to-martensite transformation due to plastic deformation. In this regard, a great deal of work has been undertaken employing quantum beams [21–26] for in-situ observation. In-situ diffraction experiments offer a rapid method of measuring carbon enrichment [23,24], internal stress / strain [21,22,24], and phase volume fractions [21–23], throughout the processing route or external loading. An in-situ high-energy X-ray diffraction (hereinafter XRD) technique was employed by Choi et al., who succeeded in obtaining the stress-strain response for each phase during a tensile test [25]. Such in-situ XRD measurements have primarily focused on obtaining averaged values and/or behaviour for relatively wide regions of interest. However, the detection of local variations, such as grain by grain variations and the existence of local gradients inside grains, has thus far remained intractable.

Recently, more direct techniques have been applied, which involve measuring morphological and crystallographic characteristics of individual grains in three dimensions (hereinafter 3D) [26,27]. With the advent of such state-of-the-art measurement techniques, it is expected that the details of the austenite-to-martensite transformation processes for practical materials with 3D complexity will be fully understood. Jimenez-Melero et al. utilized a 3D-XRD technique [26] to map 3D crystallographic orientation in real space [28], and successfully demonstrated the transformation behaviour of individual austenite grains in terms of their carbon content and grain size. As in the abovementioned reports, the transformation behaviour was found to be primarily determined by the carbon content, according to the overall pattern of increasing carbon content with decreasing austenite grain size.

Since remarkable spot blurring and spot overlap occur during plastic deformation in such XRD experiments [27], Jimenez-Melero et al. were forced to utilize cooling instead of mechanical loading in order to investigate austenite-to-martensite transformation, for reasons of experimental accuracy [28]. More recently, the present authors proposed a multi-modal technique called diffraction-amalgamated grain boundary tracking (hereinafter DAGT) [27]. X-ray tomography is capable of imaging dispersion particles and grain boundaries, enabling the reconstruction of grains in polygonal form by identifying a great number of particles located along grain boundaries. The advantage of the DAGT technique is that it enables the tracking of individual grain boundary particles throughout a given plastic deformation process, for the purpose of determining the change in grain morphology during plastic deformation. The crystallographic orientation of each grain is measured, simultaneously with the grain imaging, by employing a special XRD measurement in which a collimated X-ray beam is raster scanned, with the sample being rotated during the raster scan data collection. The DAGT technique has been successfully utilized to reveal characteristic deformation behaviour of polycrystalline aluminium alloys in 3D [27,29].

In the present study, the DAGT technique was used to quantitatively assess the role of individual austenite grains in relation to austenite-to-martensite transformation behaviour during plastic deformation. Since there are far less visible grain boundary particles in a C-Mn-Si multi-phase steel than in chemically reactive aluminium alloys, contrast-enhanced X-ray nano-tomography (hereinafter XNT) imaging of the dual phase microstructure has been utilized to directly visualize retained austenite grains. In a previous study, the spatial resolution of the phase-contrast X-ray tomography images was limited to 3.3 μm when a DP steel with a relatively small density difference between constituent phases was imaged [30]. This does not appear sufficient to depict the morphology of phases in practical steels in full 3D complexity. The present authors have, however, recently achieved 150 nm spatial resolution at a high X-ray energy of 30 keV, by developing a type of X-ray Zernike phase-contrast XNT which is effective for imaging practical steels [31]. In the present study, this technique was for the first time utilized for in-situ observation of the deformation and transformation behaviour of a steel.

2. Experimental

2.1. Material used

A C-Mn-Si multi-phase steel with a chemical composition of 0.1 C, 5 Mn, 1 Si, and balance iron in mass% was prepared. A cold rolled steel plate was subjected to intercritical annealing at 933 K for 400 h, followed by water-quenched to room temperature to obtain granular retained austenite. C-Mn-Si multi-phase steel consists of a retained austenite phase interconnected in a reticulate manner, and a matrix ferrite (Fig. S1 (a) and (b)). The volume fraction of the retained austenite phase is 22.1%. The interconnected retained austenite phase is divided, by transverse grain boundaries, into austenite grains of approximately 3 μm in equivalent sphere diameter (Fig. S1 (b)). The carbon content is inhomogeneous in each retained austenite grain (i.e., there are locally high-carbon-content regions scattered inside each grain, as shown in Fig. S1 (c)), and also remarkably different grain by grain. The density difference between the austenite and ferrite, calculated from measured local chemical compositions, is approximately 1.7%. The M_s temperature, calculated from the local carbon content, is 20.1 °C [14], and the M_s^{σ} temperature of C-Mn-Si multi-phase steel has been reported to be −5 to 20 °C [14], which is not sensitive to chemical compositions [32]. The M_s^{σ} temperature of the steel used here was therefore estimated to be close to 20 °C, which implies

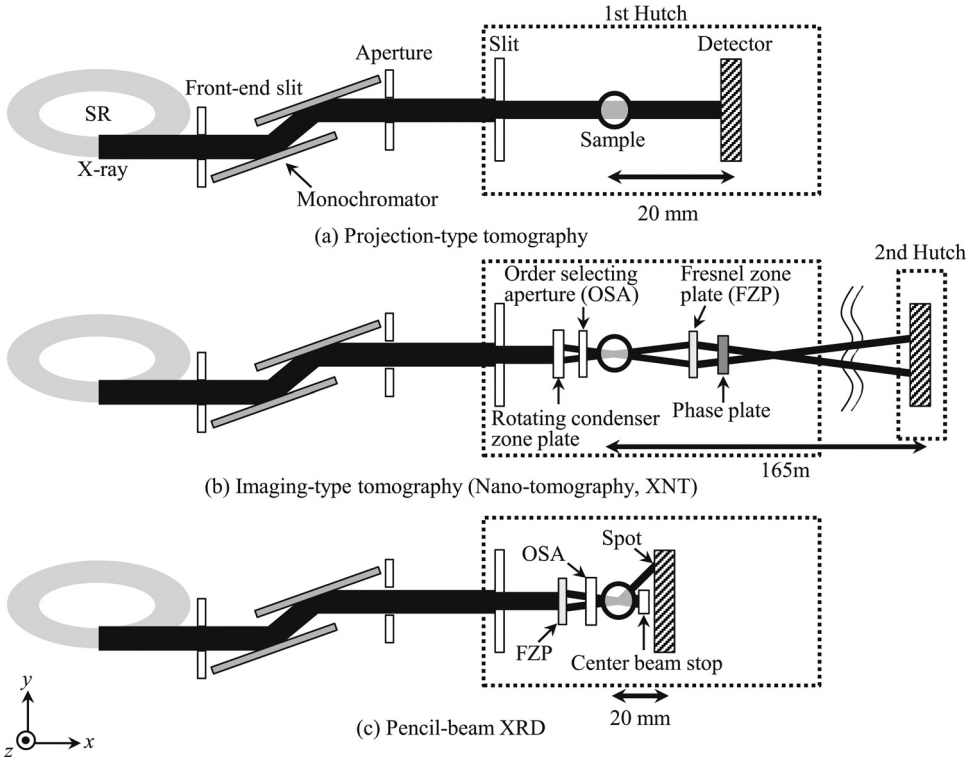

Fig. 1. Schematic illustrations of the three set-ups for the X-ray nano-tomography and pencil-beam XRD experiments in a synchrotron radiation facility.

that the retained austenite phase of the present material was comparatively unstable for C-Mn-Si multi-phase steels.

Two in-situ tensile specimens (Fig. S2) were sampled in parallel to the rolling direction, using the electro discharge machining technique. An initial 1 mm × 1 mm square gauge section was then electro polished to produce a nearly cylindrical gauge section of about 0.1 mm in diameter.

2.2. Synchrotron experiments

Both the XNT and XRD experiments were performed at BL20XU of SPring-8. The major conditions for the synchrotron experiments are summarized in Table S1. Two experiments, several months apart, were approved by SPring-8. In the first beamtime (Experiment 1), XRD experiments were conducted as shown in the stress-strain curves in Fig. S3; XRD was measured only in the initial unloaded state for Specimen A, but was repeated six times, along with the stress-strain curve, for Specimen B. A projection-type X-ray micro-tomography setup (Fig. 1(a)) was placed side-by-side with the XRD or XNT setup at BL20XU, to match the region of interest for both experiments. In the second beam time (Experiment 2), Specimen A was loaded and its deformation and transformation behaviour observed using the XNT technique.

Note that the stress-strain curves (especially the elastic regions) in Fig. S3 differ from the actual material response due to the relatively low stiffness of the miniature material test rig specially designed for synchrotron experiments. This is because a relatively thin polymer tube is used as a load frame in consideration of its transmittance. Significant stress relaxation, which inevitably causes drift of regions of interest, was also observed in Fig. S3 in both experiments. Microstructural patterns, such as particles and pores, that were visible in the projected versions of the XNT images (at both 0 and 90° of sample rotation angle) were tracked throughout the tensile tests to capture diffraction spots/3D images from exactly identical regions throughout the tensile tests.

2.2.1. XNT experiments (Experiment 2)

The entire specimen was imaged using the projection-type X-ray micro-tomography technique, to identify the region of interest for XRD measurement in Specimen A; and then the XNT technique was employed at a higher magnification, to observe the region of interest. A monochromatic X-ray beam of 20 keV was produced by a liquid nitrogen-cooled Si (111) double crystal monochromator. The miniature material test rig was positioned approximately 80 m from the X-ray source.

For the projection-type X-ray micro-tomography (Fig. 1(a)), a CMOS camera (ORCA Flush 4.0, Hamamatsu Photonics K. K.) of 4.0 megapixels was combined with an objective lens and a 20-μm thick GAGG ($Gd_3Al_2Ga_3O_{12}$: Ce^+) scintillator to set an effective pixel size of 0.5 μm × 0.5 μm and a spatial resolution of 1.0 μm in the reconstructed slices. The sample-to-detector distance, L, was 20 mm. The exposure time for each projection was 0.15 s. A total of 1800 projection images were captured to reconstruct a single 3D image.

In the XNT Experiment, a characteristic large-scale X-ray microscope was used, with L of 165 m, as shown in Fig. 1(b). Köhler illumination [33] with a rotating condenser zone plate was used to establish the imaging-type XNT setup with Zernike phase-contrast mode [33]. An annular aperture was placed in front of the condenser zone plate. A specially designed Fresnel zone plate (hereinafter FZP) for high X-ray energy (i.e., apodization FZP [33]), 310 μm in diameter and 150 nm in outermost zone width, was used. The focal length of the FZP was 500 mm, and the diffraction efficiency was 9.1% at 20 keV. The FZP was located 500 mm downstream from the sample, and an annular phase plate was placed at the back focal plane of the objective FZP (i.e., 500 mm from the FZP), thereby providing the phase shift necessary for the Zernike phase-contrast X-ray microscope [33]. The FZP, the sample and the phase plate were set in the first experimental hutch. The same CMOS camera was combined with an objective lens and 200-μm thick LuAG($Lu_3Al_5O_{12}$:Ce^+) powder scintillator, and set in the second experimental hutch, in a building separate from the SPring-8

main ring building. The exposure time was 0.5 s. The XNT technique provided isotropic voxels with 0.061 μm edges (2 × 2 binning applied) and a spatial resolution of 0.16 μm in the reconstructed images. The spatial resolution values were directly measured in the reconstructed slices by measuring edge responses at visible interfaces in the specimens [33]. A total of 3600 projection images were captured to reconstruct a single 3D image. In both experiments, image slices were reconstructed from a series of projections based on the conventional filtered backprojection algorithm.

2.2.2. XRD experiments (Experiment 1)

The same CMOS camera was also combined with a 20-μm thick P43 (Gd_2O_2S:Tb^+) powder scintillator, and set 20 mm downstream from the specimens. The specimens were placed at the back focal plane of the objective apodization FZP (Fig. 1(c)) to collimate the monochromatic beam to form an X-ray pencil beam. The X-ray pencil beam was raster scanned (50 rows and 50 columns in 1 μm increments) with the samples being rotated over 180° in 1° increments during the raster scan data collection, resulting in a total of 450 000 diffraction patterns (i.e. roughly twenty-five million diffraction spots in total in it) being captured for each loading step. The exposure time was 0.03 s/pattern. Since the X-ray beam was collimated down to a micron-level [2.7 / 3.4 μm (vertical / horizontal directions) and 1.5 / 2.0 μm (ditto) for full width at 50% and 75% of maximum, respectively] through use of the specially designed FZP, crystallographic orientation mapping was successfully realized. The X-ray energy was tuned to 37.7 keV to capture diffracted spots from the γ (111), (200), and (220) planes, and parts of the γ (311) and (222) planes (Fig. S4). The effect of spot blurring due to retained austenite grain size along the X-ray beam direction provides little contribution to the accuracy of spot broadening measurements, accounting for approximately 1% of the average full width at half maximum values.

2.3. Image analysis

2.3.1. XNT images (Experiment 2)

3D median filtering was applied for noise reduction. Adaptive thresholding [34] was then applied for segmentation of the XNT images, due to the spatial variations in the grey value levels originating from artefacts. The threshold level required for the adaptive thresholding was determined such that the volume fraction of the retained austenite phase agreed with that obtained by cross-sectional EBSD measurement (i.e., 22.1%).

The grain boundaries of the retained austenite are not visible in the XNT images, as the XRD data was too coarse to accurately identify the location of these boundaries. The watershed algorithm was therefore applied, to distinguish the austenite grains in the XNT images (e.g., Fig. S1 (b)) [33]. The H-minima transform was also applied, to overcome over-segmentation during the watershed treatment [33].

2.3.2. XRD images (Experiment 1)

To suppress inaccuracies originating from image noise, only diffraction spots over eight pixels in the diffraction patterns were extracted for the subsequent analysis. Since the collimated beam size is to some extent smaller than the actual grain size, a diffraction spot originating from a specific grain was consecutively observed for each rotation angle during the raster scan data collection (e.g., Fig. S5 (a) - (c)). This provided projected grain images (e.g., Fig. S5 (a) - (c)) for which each diffraction spot in the XRD data corresponded to a retained austenite grain observed using the XNT technique, based on their spatial consistency (i.e., each diffraction spot was back projected to the position occupied by a specific grain observable in a corresponding XNT image). The details are available elsewhere [27]. A pair of scattering vectors was used to calculate the crystallographic orientation of each grain. Three pairs (i.e., combinations of the three low angle planes; (111), (200), and (220) planes) were in most cases available for each grain. Only when three crystallographic orientations, as calculated from the three pairs, fell within 0.5° was an average orientation assigned to the corresponding grain, in order to ensure the accuracy and reproducibility of the measurement.

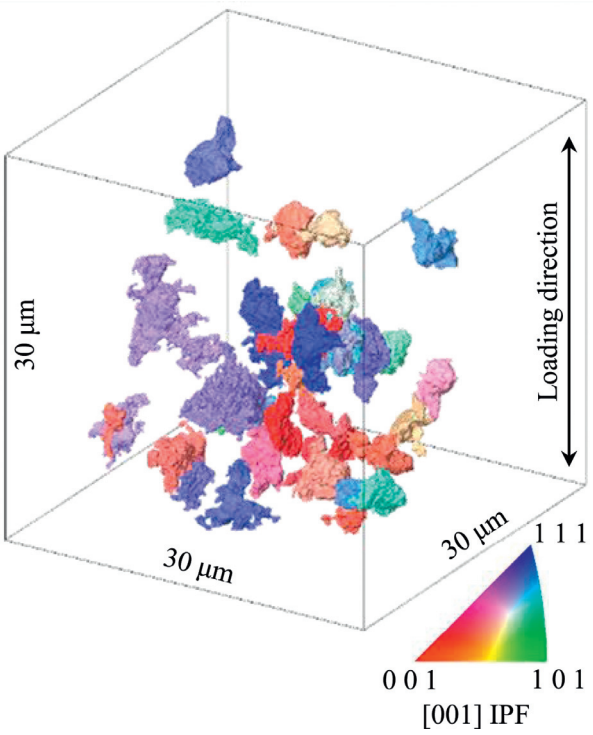

Fig. 2. 3D morphology and crystallographic orientation of each of the 46 grains that were embedded in the 30 × 30 × 30 μm unit box for Experiment 2. The colour code in the 3D image corresponds to the [001] inverse pole figure in Fig. 7.

The three pseudoprojected images of grains that originated from the three low angle planes (e.g., Fig. S5 (a) - (c)) were also used for reconstructing 3D retained austenite grains (e.g., Fig. S5 (d)). Although, due to the limited number of projections (only 3), this reconstruction is very crude compared to the high-resolution XNT images (3600), the data is nonetheless valuable for evaluating interactions amongst neighbouring austenite grains when considering the dislocation density, crystallographic orientation, and mechanical driving force, as well as changes in their values during loading, which were obtained in Experiment 1. The beam paths for the three pseudoprojected images inevitably overlap at the location of an original grain, which is also beneficial for eliminating incorrect matching, both amongst the three pseudoprojected images and between the XRD data and XNT grain images.

The modified Williamson-Hall method was used to calculate the dislocation density for each diffraction spot [35], and the average dislocation density calculated for the three low angle planes was assigned to the corresponding grain.

3. Results

3.1. Image-based analysis (Experiment 2)

Fig. 2 shows the 3D morphology and initial crystallographic orientation of all the retained austenite grains. Complex austenite morphology is observable in the figure, and there is clearly a rolling texture; the majority of the retained austenite grains are orientated so that the ⟨111⟩ direction (blue in the figure) is roughly

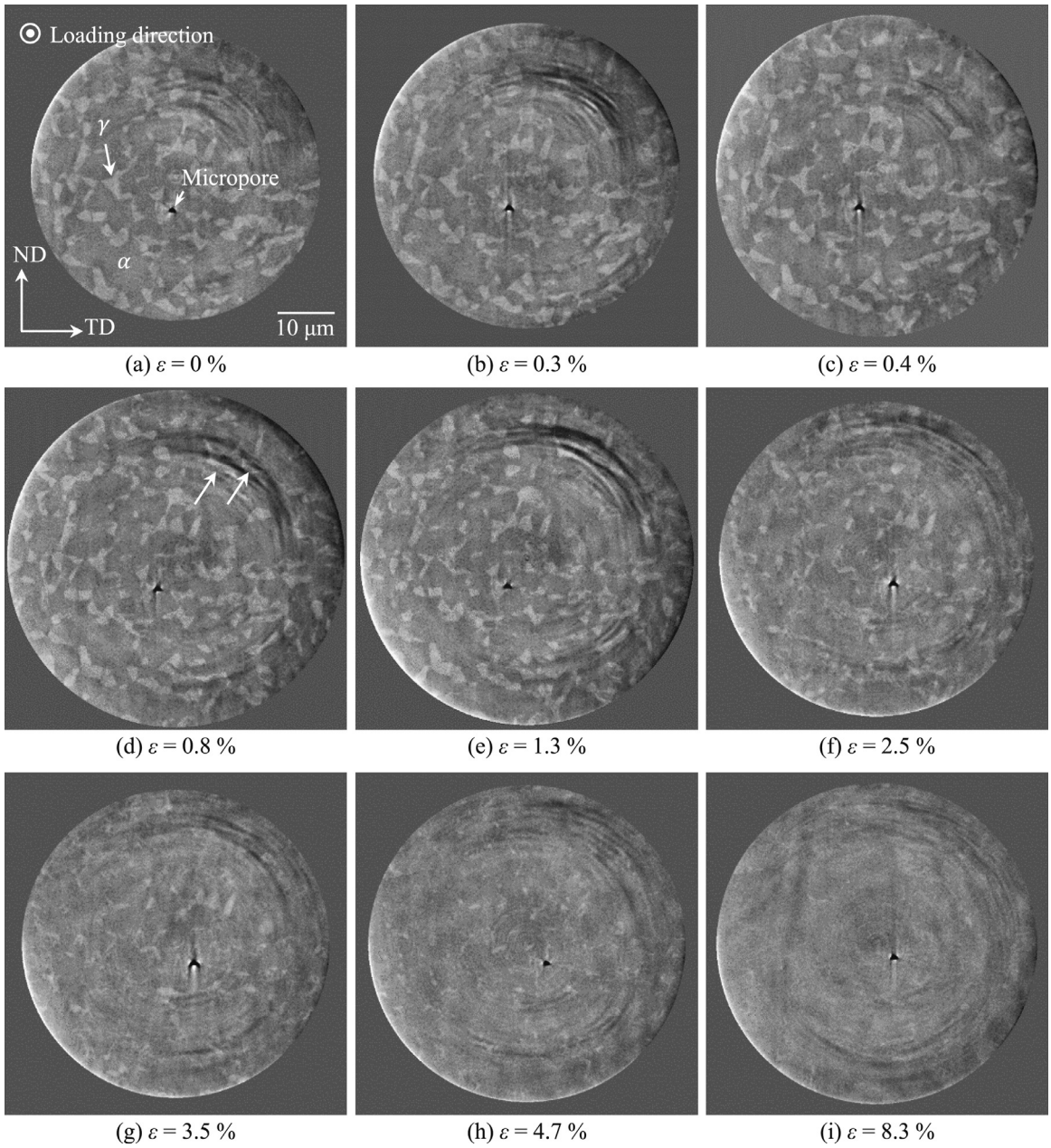

Fig. 3. Annihilation of the retained austenite phase, γ, during external loading in Experiment 2. An identical transverse virtual cross-section is shown in a series of nano-tomography images. Note that the martensite phase was invisible with the present set-up due to its very small density difference from the ferrite phase, α.

parallel to the tensile direction, and many of the remaining grains are accumulated around the ⟨001⟩ direction (red in the figure). A few grains are present around the ⟨101⟩ direction. The overall annihilation behaviour of the retained austenite phase during loading is shown, in Fig. 3, as the changes in an identical virtual cross-section, which are summarized as the black solid circles in Fig. 4(a). Although arc-shaped ring artefacts are more or less observed, as highlighted by arrows in Fig. 3(c), the morphological change in the retained austenite is clearly seen in Fig. 3. Notably, as the figure suggests, the martensite phase was invisible with the present set-up, due to its very small density difference from the underlying ferrite phase. The onset of the austenite-to-martensite transformation is seen between the applied strain of 0.3 - 0.4%, which roughly corresponds to the yield stress. A marked reduction in the retained austenite volume fraction clearly occurs between 0.3 - 3.5%, and only a limited number of small segments are sparsely scattered at 4.7%. Some of the coarse retained austenite grains remained until an applied strain of 2.5 - 3.5%, and almost complete annihilation is observed at 8.3%, which corresponds to the loading step immediately after the maximum stress is reached. Although the macroscopic strain level at which transformation occurred is different, this rapid transformation closely agrees with the reported tendency (e.g., 0.15C-10Mn-1.5Al-0.2Si and 0.22C-1.8Mn-0.04Al-1.4Si multi-phase steels in ref. [36]). Deformation and transformation occurred homogeneously up to necking, whereas propagative instabilities with Lüders and Portevin-Le Châtelier-like bands, reported in 0.15C-10Mn-1.5Al-0.2Si multi-phase steel [36], were not observed in the present study.

An example of the austenite-to-martensite transformation of individual grains is shown in Fig. 5. Localized transformation, which is indicated by an arrow in Fig. 5(a) is observed at an applied strain of 1.3% for the green grain. The local transformation then

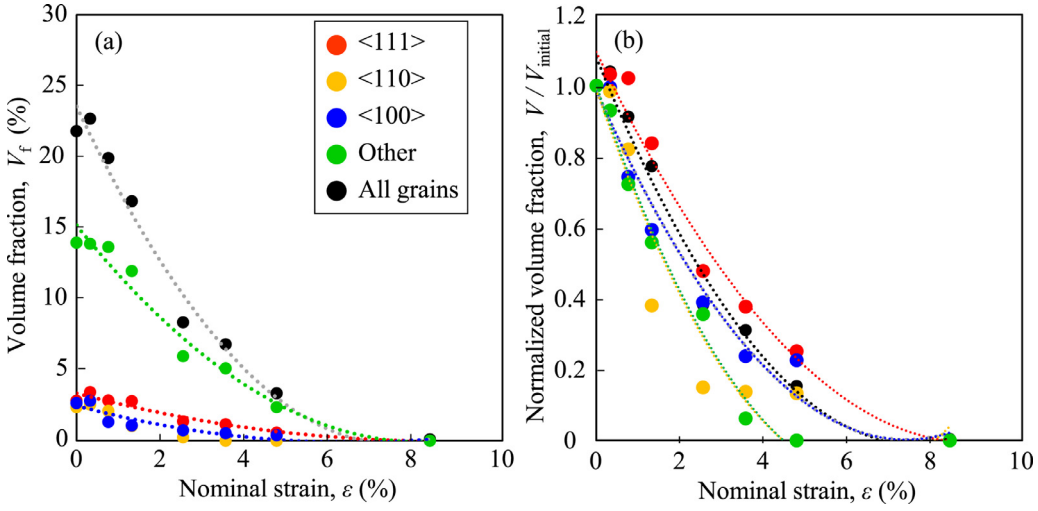

Fig. 4. Variation in (a) the volume fraction and (b) the volume fraction normalized with each initial volume fraction of the retained austenite phase, with applied strain in Experiment 2. The red, yellow, and blue circles indicate retained austenite grains with initial grain orientations to the tensile axis within 15° of the ⟨111⟩, ⟨110⟩, and ⟨100⟩ directions, respectively (green circles denote the remaining orientations). Black circles indicate the sum of all the grains.

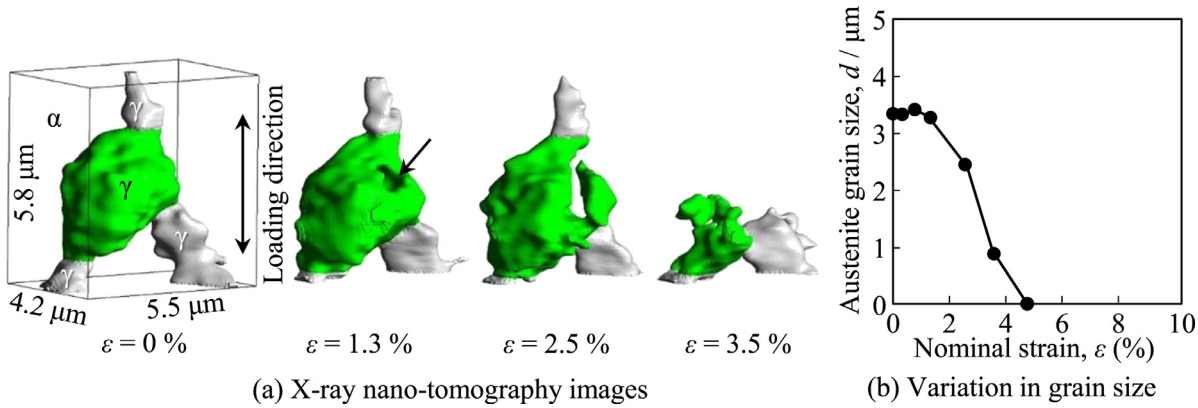

Fig. 5. (a) Typical example of austenite-to-martensite transformation during loading in Experiment 2, together with the variation in grain size of the grain shown in (a) expressed in terms of equivalent sphere diameters. The green retained austenite grain was connected to the three adjacent austenite grains highlighted in grey.

propagated, eroding vertically into a wedge-shape at 2.5%, followed by an abrupt transformation between 2.5 and 3.5%. It is also observed that an upper adjacent austenite grain (highlighted in grey) transformed at roughly the same time as the green austenite grain, whereas the lower right austenite grain (also highlighted in grey) remained up to 3.5%, implying a variety of transformation behaviour for individual grains.

The change in austenite volume fraction was classified according to the initial crystallographic orientation in Fig. 4(a), while the annihilation rates are readily comparable in the normalized data in Fig. 4(b). Close inspection of Fig. 4(b) reveals that the retained austenite grains with a tensile axis within 15° of their initial ⟨110⟩ direction exhibit rather rapid transformation, whereas those within 15° of the initial ⟨111⟩ direction exhibit a below-average transformation rate. Fig. 4(b) also reveals that the onset of the transformation was retarded in the case of the grains with a ⟨111⟩ orientation, whilst rapid transformation occurred immediately after the onset of loading for the grains with a ⟨110⟩ orientation. Fig. 6 shows the transformation behaviour of all 46 grains whose initial crystallographic orientations were successfully identified using the XRD data. In addition to the effects of the initial crystallographic orientation (Fig. 4), coarse austenite grains are prone to slow transformation, with the external strain level at which the austenite grains fully transformed to martensite almost doubled in the case of coarse (more than 3 μm in diameter) versus fine (less than 2 μm) austenite grains. Gradual shrinkage is observed, especially in the case of coarser grains; whereas, in the case of smaller austenite grains, transformation tends to be initiated later, after the grain size has been maintained for a while, or immediately after the onset of loading in the case of the remaining small austenite grains.

3.2. Diffraction-based analysis (Experiment 1)

Fig. 7, which shows the crystallographic orientations of all 58 austenite grains that were obtained by crystallographic analysis of the XRD data, reveals that their crystallographic orientations were successfully identified throughout transformation. The rolling texture observed in Fig. 2 (the majority of retained austenite grains present near to the ⟨111⟩ orientation) is also confirmed here. The arrows in Fig. 7 indicate rotation paths during transformation. When the transformation is protracted up to an applied strain of 3.5% or above, the majority of the grains are rotated to a non-negligible extent; for example, 2.0° in rotation angle on average for an applied strain range of 5.8%. It is also noteworthy that some of the grains reversed their paths in the middle of transformation; for example, the typical reversal by the grain circled in black in the figure.

The respective variations in dislocation density in the retained austenite grains are summarized and classified according to the

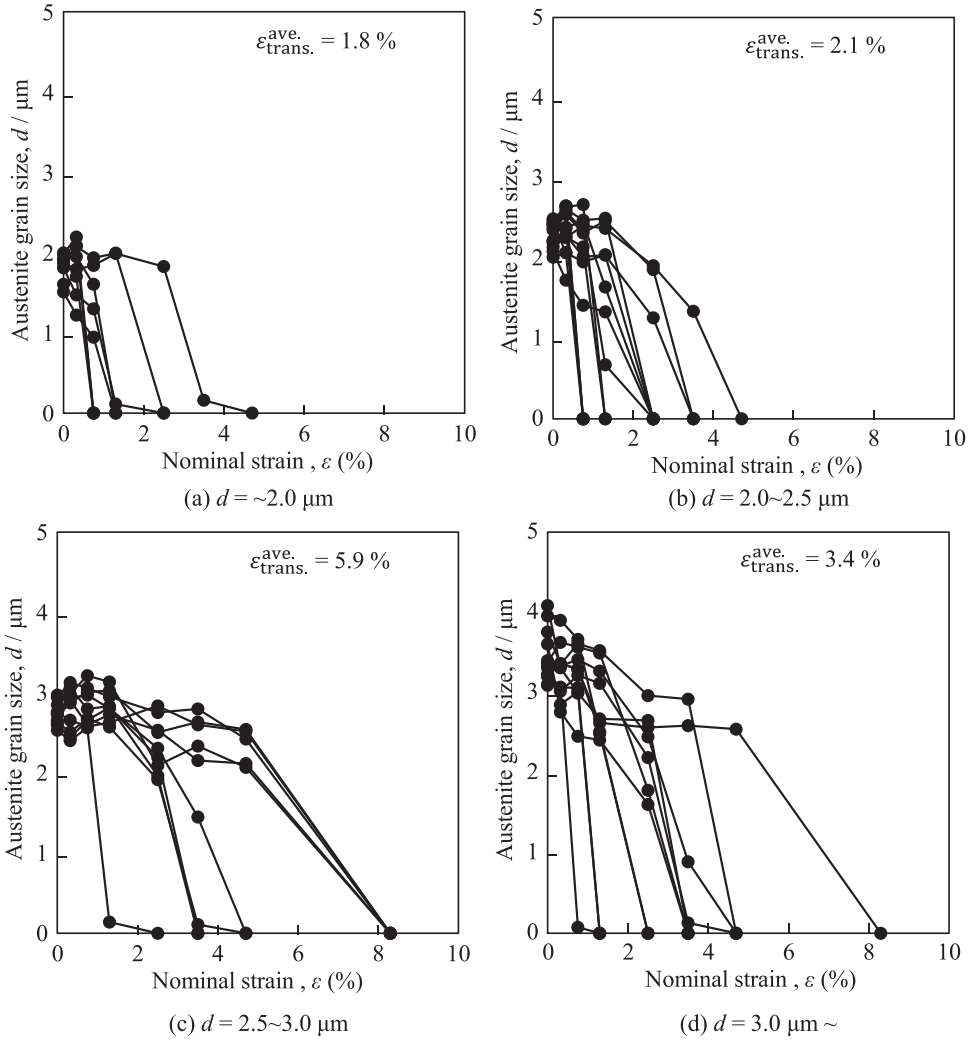

Fig. 6. Change in the equivalent sphere diameter of retained austenite grains with applied strain. All 46 austenite grains that were successfully identified in Experiment 2 were classified according to their equivalent sphere diameter. The external strain levels at which the austenite grains fully transformed to martensite are averaged and shown as $\varepsilon^{ave.}_{trans.}$ in (a) to (d).

initial grain orientations in Fig. 8. Although there seems to be a wide variation in initial dislocation density and subsequent multiplication behaviour in Fig. 8(a), the averaged data shown in Fig. 8(b) clearly demonstrates that the dislocation multiplication behaviour of austenite grains is strongly affected by their crystallographic orientation; the austenite grains close to the ⟨111⟩ orientation exhibit a rather gradual increase in dormant dislocation density, whereas those close to the ⟨110⟩ orientation exhibit rapid multiplication. The ⟨100⟩ direction appears to represent an intermediate tendency between the ⟨111⟩ and ⟨110⟩ directions.

In order to confirm the relationship between the austenite-to-martensite transformation and plastic deformation for individual grains, seven characteristic grains were extracted (Fig. 9), to illustrate the variety of behaviour observed during the increase in dislocation density and transformation. It is evident that rapid transformation is apt to occur for austenite grains that exhibit abrupt dislocation density increase (grains G1, G3, and G6), whereas those with moderate dislocation density increase (grains G2, G4, and G5) tend to show slow and gradual transformation, while grain G7 appears to illustrate an intermediate tendency. In Figs. 10, S6, and S7, these tendencies are interpreted in terms of the mechanical driving force and Schmid factor.

The mechanical driving force, U, is the driving force necessary for the stress-assisted transformation that occurs between M_s and M_s^{σ}, which compensates for the lack of chemical driving force. It has typically been estimated as the work done by applied stress, as follows [37]:

$$U = \tau\gamma_0 + \sigma_N\varepsilon_0, \tag{1}$$

where τ and σ_N are the resolved shear stress and normal stress acting on the habit plane of martensite, respectively. γ_0 is the transformation shear strain along a transformation shear direction on the habit plane, and ε_0 is the dilatational strain in the direction normal to the habit plane. The mechanical driving force is described for uniaxial tension with a tensile stress of σ_a as follows:

$$U = \frac{1}{2}\sigma_a\gamma_0 \sin 2\theta \cos\alpha \pm \sigma_a\varepsilon_0(1+\cos 2\theta), \tag{2}$$

where θ is the angle between the tensile axis and the normal to the habit plane, and α is the angle between the transformation shear direction and the maximum shear direction on the habit plane. These equations imply that the austenite-to-martensite transformation is dependant on the local stress state, and differs grain by grain according to the grain orientation with respect to the tensile direction. The maximum mechanical driving force is generated for the maximum shear direction (i.e., $\alpha = 0$). The values of γ_0 and ε_0 for C-Mn-Si multi-phase steel are available in the literature: $\gamma_0 = 0.26$ and $\varepsilon_0 = 0.03$ [38]. These yield

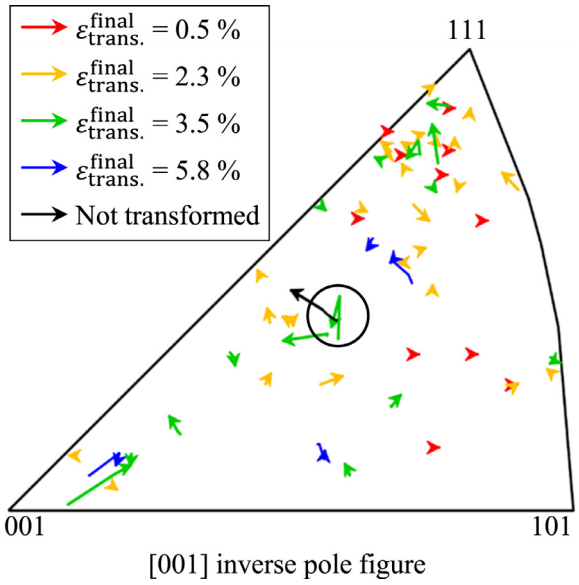

Fig. 7. Crystallographic orientation distribution and rotation behaviour on a [001] inverse pole figure. All 58 austenite grains that were successfully identified in Experiment 1 are colour-coded according to the external strain level at which the austenite-to-martensite transformation is completed.

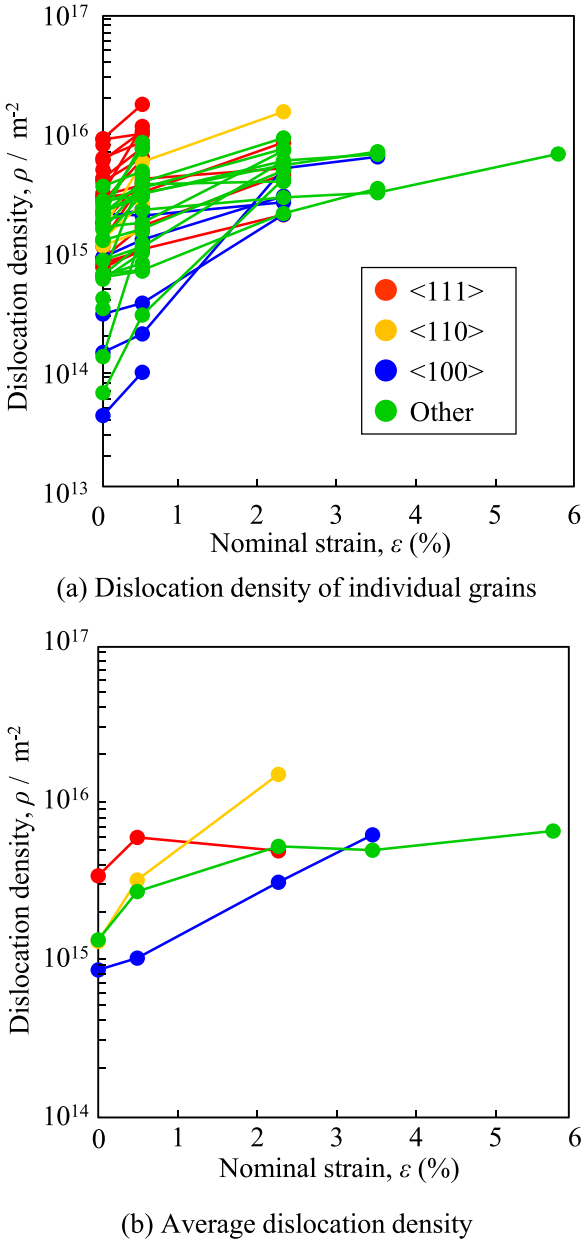

Fig. 8. Change in the dislocation density of retained austenite grains with applied strain. All 58 austenite grains that were successfully identified in Experiment 1 are classified, in (a), according to their initial grain orientation to the tensile axis: within 15° of the ⟨111⟩, ⟨110⟩, and ⟨100⟩ direction, and other. (b) shows the change in average values.

the first transformation in the austenite grains with $\theta = 42^{\circ}$, provided that the local tensile stress acting on the individual grains is uniform. Since the present discussion focuses mainly on the early stage of the austenite-to-martensite transformation, butterfly-type martensite with its habit plane of {225}, which is nucleated prior to lath martensite formation [39], is assumed in this analysis.

The mechanical driving force and Schmid factor were calculated for the initial and the final stages of the transformation (Fig. S6), and there was no conclusive evidence that either of these factors was predominant in the plastic deformation or transformation. Rapid dislocation density increase is observed for the austenite grains with lower Schmid factors (e.g., grains G1 and G3 in Fig. S6 (b)), and transformation retardation is observed for the austenite grains with relatively higher mechanical driving forces (e.g., grain G2 in Fig. S6 (a)). We then focused on the two early loading steps at which almost all the grains exhibited the onset of transformation (Figs. 10 and S7). At an applied strain of 0.5%, the austenite grains with higher driving forces are prone to commence transformation (Fig. 10). The austenite grains orientated within 15° of the ⟨111⟩ orientation are especially likely to show higher mechanical driving forces. This is followed by the reduction in mechanical driving forces at the later 2.3% applied strain. On the other hand, there is little evidence of a Schmid factor effect on the initial transformation behaviour (Fig. S7).

It would be of significant value if the visualization of interaction behaviour could help us understand both the discrepancy between the averaged data (Fig. 10) and the data for individual austenite grains (Fig. S6), and the wide dispersion of data for individual austenite grains shown in Figs. 6,8,9, and 10. Fig. 11 shows the interaction amongst grains G5 - G7 in Fig. 9. These grains are adjacent to each other, and their crystallographic orientations are relatively similar, with misorientation angles of 35.8°, 7.9° , and 38.1° for the G5-G6, G6-G7, and G7-G5 grain combinations, respectively. Grain G6, with a fairly high mechanical driving force, first transformed to martensite at an applied strain of 2.3%, which was followed by the rather gradual transformation of grain G7. Grain G5 was similar to grain G7 in orientation, and had a relatively high mechanical driving force and Schmid factor. Of the 58 grains, however, only grain G5 was not completely transformed up to an applied strain of 8.7%. Grain G5 was surrounded by hard martensite plates originating from grains G6 and G7 at 2.3% applied strain. It is therefore reasonable to assume that these neighbouring plates caused the retardation in the G5 transformation, due to strong deformation constraint; and this would appear to bear some affinity with the rather gradual dislocation density increase in G5, seen in Fig. 9. Although it seems likely that the internal stress in the martensite grains increased with the plastic deformation of the neighbouring austenite grains, no damage was observed in the martensite grains. This is attributable to the strength of fresh martensite, which is greater than that of the aged martensite in DP steels for example. Another point to note is the considerable rotation of grain G5, and accompanying reduction in the Schmid factor, during transformation (Fig. S6 (b)). Grain G5 was rotated by 7.2° towards (113) plane between an applied strain of 0

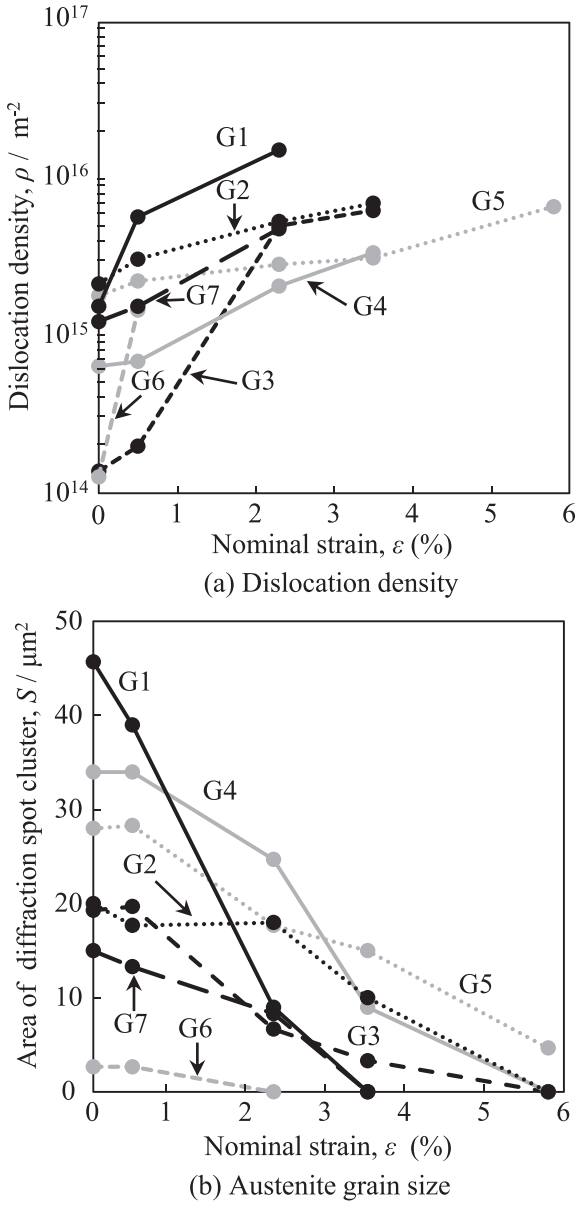

Fig. 9. Change in (a) the dislocation density and (b) the retained austenite grain size, with applied strain. Seven characteristic grains (G1 – G7) have been extracted from the total number of grains obtained in Experiment 1. The retained austenite grain size is expressed as the average of the projected spot-cluster areas obtained for three incident beam orientations; diffractions from the {111}, {200}, and {220} planes.

and 5.8%, while its rotation was limited to 2.0% after the cessation of the transformation in grain G7 at applied strain of 3.5%.

4. Discussion

4.1. Transition of transformation mechanisms

The stress-assisted and strain-induced transformation mechanisms prevail at stress levels lower and higher than the yield stress of austenite, respectively [16] (or in other words, at test temperatures lower or higher than M_s^{σ}). It is therefore reasonable to assume that the two mechanisms operate alternately; in many cases, the strain-induced transformation is expected to enhance the ductility-strength balance [14]. In this study, though the data for individual grains was more or less dispersed, as will be discussed later, the early stage of the austenite-to-martensite transformation was associated with the mechanical driving force, whereas the overall transformation was interrelated with dislocation multiplication. This implies that the former was dominated by the

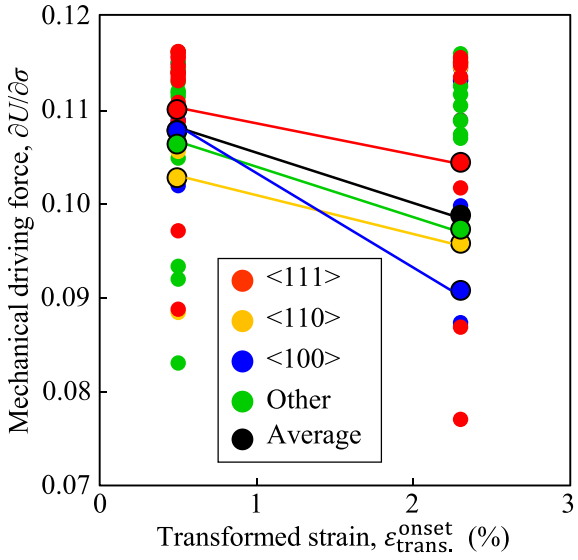

Fig. 10. The mechanical driving force, U, for austenite-to-martensite transformation, expressed as $\partial U/\partial\sigma$, a function of the nominal strain at which the transformation commences, for each grain. All 58 austenite grains that were successfully identified in Experiment 1 are classified according to their initial grain orientation to the tensile axis: within 15° of the ⟨111⟩, ⟨110⟩, and ⟨100⟩ direction, and other; together with the average values for all the grains.

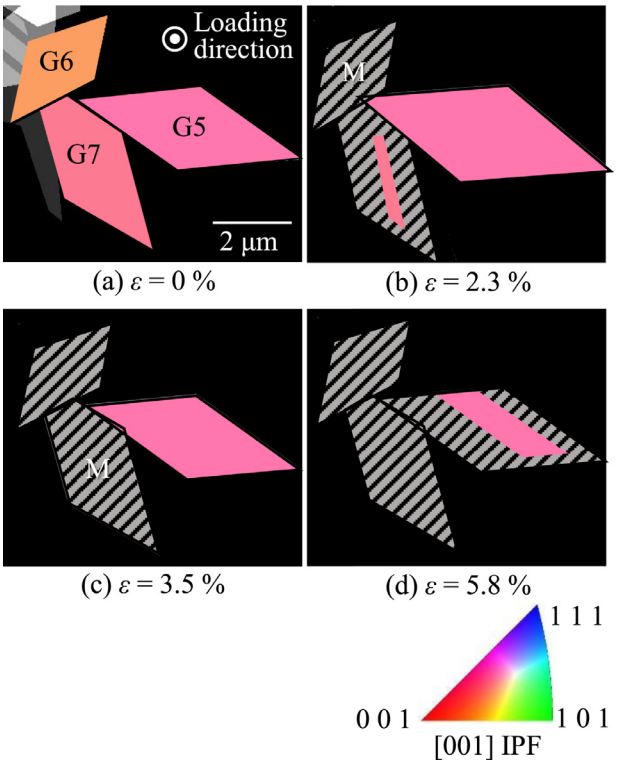

Fig. 11. Characteristic interaction amongst neighbouring retained austenite grains displayed by coarsely reconstructing the morphologies of the grains only from the X-ray diffraction data obtained in Experiment 1. Three projections were used for the reconstruction. Austenite grains G5 - G7 (shown in Fig. 9) are displayed. The colour code for the retained austenite grains corresponds to the [001] inverse pole figure in Fig. 7, while the hatched grains represent martensite (M) plates transformed from austenite.

stress-assisted transformation mechanism, while the latter may be explained in terms of the strain-induced transformation mechanism. The reason why the two mechanisms were observed in the same material at the same time is the relatively low stability of the C-Mn-Si multi-phase steel used in this study (i.e., test temperature close to $M_s{}^{\sigma}$). The austenite-to-martensite transformation was observed up to an applied strain of 5.8%, which is not necessarily exceptional compared to the other C-Mn-Si multi-phase steels reported (e.g., more than 90% of the initial austenite was transformed at an applied strain of 5% in Chiang's 0.17C-1.53Si-1.5Mn steel [20]).

In terms of the onset of the austenite-to-martensite transformation, it has been generally understood that the austenite phase has higher yield strength, which is followed by higher hardening rate, than the ferrite phase, as was demonstrated by Jacques et al. [13] for a 0.29C-1.41Si-1.42Mn steel, by employing neutron diffraction and digital image correlation. Tsuchida et al. reported that blocky austenite grains, such as those observed in the present study, exhibit a greater difference in phase strain between ferrite and austenite than needle-like austenite grains [40]. It is therefore reasonable to assume that the austenite phase can undergo stress-assisted martensite transformation even after the macroscopic yielding. As shown in Fig. S1 (d), a transformed grain contains a number of martensite plates, which induces stress relaxation around subsequently transforming martensite plates, which in turn hinders the formation of the next martensite plates [41]. In addition to this, the formation of earlier martensite plates exerts geometrical constraint on the transformation of subsequent plates [41]. These factors are in qualitative agreement with the gradual transformation of individual austenite grains observed in Figs. 5,6, and 9, and it seems most likely that subsequent strain-induced transformation would be inevitable for this reason.

4.2. Dominant factors of transformation

4.2.1. Mechanical driving force and schmid factor

Haidemenopolos et al. provided the relationship between stress triaxiality, $\frac{\sigma_h}{\bar{\sigma}}$, and the mechanical driving force, as follows [42]:

$$\frac{\partial U}{\partial \bar{\sigma}} = -0.715 - 0.3206\frac{\sigma_h}{\bar{\sigma}}, \tag{3}$$

where $\sigma_{\ h}$ is the hydrostatic stress and $\bar{\sigma}$ is the equivalent stress. The mechanical driving force is reduced when the stress triaxiality is reduced with the nucleation of the martensite adjacent to austenite grains, and this would effectively reduce the rate of the austenite-to-martensite transformation. It can, however, be inferred that martensite variants that match the orientation of the surrounding ferrite matrix are preferentially chosen [43], which might impair the relationship governed by the mechanical driving force.

In terms of the strain-induced transformation stage, it has been generally understood that martensite variants nucleate on slip planes with a high Schmid factor in austenite that preferentially undergoes plastic deformation [43]. However, austenite grains with high Schmid factors did not necessarily show transformation to martensite in the present study (Figs. S6 and S7). Some of the high Schmid factor grains were rotated instead, which sometimes resulted in the Schmid factor reduction shown in Fig. S6 (b). It is inferred that the Schmid factor reduction is more or less attributable to the retardation in transformation. The results should, however, be interpreted with caution; Tirumalasetty et al. pointed out that such rotations are observed preferentially within single ferrite grains because the stress state around austenite grains embedded in larger ferrite grains is rather uniform (and therefore relatively suppressed compared to stress-localized regions), resulting in rotation before the commencement of phase transformation [19]. In addition to the rapid disappearance of <110>-orientated austenite grains due to transformation, deformation texture formation is apt to occur both in the ferrite and austenite phases. It is well known that the ferrite and austenite phases are prone to form ⟨110⟩ and ⟨111⟩ tensile fibre textures, respectively [44]. It is also well understood that the retained austenite grains satisfy the Kurdjumov-Sachs orientation relationship with the underlying ferrite matrix (i.e., $(111)\gamma$ // $(110)\alpha$ and $[110]\gamma$ // $[111]\alpha$) [43]. This relationship might be maintained during tensile deformation such that both phases deform coordinately. There were, however, qualitative differences from the data shown in Fig. 7, where no obvious texture formation tendency is observed. It can be inferred that the austenite grains are too unstable to demonstrate such preferential orientation behaviour under the relatively low plastic strain.

The influence of another factor, the stress partitioning mechanism, should also be taken into account; the interactions with surrounding phases can cause local stress elevation, thereby limiting the direct consequence of the Schmid factor.

4.2.2. Austenite grain size

It has been well documented that the refinement of austenite grains increases their stability [15,16,18], and this has been phenomenologically postulated based on the following two viewpoints: coarse austenite grains are prone to have a number of pre-existing martensite nuclei, thereby accounting for their lower stability [18]; and the interfacial energy at an interface between an emerging martensite and residual austenite acts as an energy barrier [18]. These posited phenomena are associated with both the stress-assisted and strain-induced martensite transformation mechanisms. Based on their model analysis, Haidemenopoulos et al. concluded that the stability enhancement due to the refinement in austenite grain size is mainly attributable to retardation in the strain-induced transformation kinetics [16]. In contrast to these reports, Fig. 6 clearly shows that coarse austenite grains exhibited prolonged transformation, which is usually beneficial for the strength-ductility balance. It should be noted here that, in the current literature, austenite grain size typically ranges between 0.1 and 1 μm, whereas, in the present study, it exceeded 1.5 μm (approximately 4 μm at the maximum). Since the sampling volume increases by two orders of magnitude with an increase in average grain volume from 0.6 μm (i.e., the optimum retained austenite grain size proposed by Cai et al. [15]) to 3 μm (the average austenite diameter in this study), it is reasonable to conclude that the claims alluded to above must be questioned.

Takaki et al. revealed, on the basis of the elastic strain energy required for martensite nucleation, that multi-variant transformation does not occur when austenite grains are refined to 1 μm or less, suppressing martensitic transformation in metastable austenite [45]. This is consistent with the microstructural features here observed after transformation (Fig. S1 (d)); the grain size of all the austenite grains well exceeded 1 μm in the C-Mn-Si multi-phase steel used in the study. It is reasonable to assume that, during the formation of multi-variant martensite from a coarse and blocky austenite grain, not all the variants are simultaneously formed; variant selection occurs based on the mechanical driving force, Schmid factor, and/or reduction in the interfacial energy between ferrite and martensite (as discussed by Yamashita et al. [43]). For example, Miyamoto et al. reported that, of 24 possible martensite variants, 6 selected variants that satisfied the relationship, $(011)\alpha//(111)\gamma$ (i.e., the primary slip plane of γ),), were preferentially formed under a relatively low applied strain of 10% [46]. The formation of earlier variants exerts stress relaxation and geometrical constraint on the growth of subsequent variants [41], thereby resulting in the gradual transformation observed in the present study.

In addition, Haidemenopoulos et al. investigated the effects of stress triaxiality changes and average austenite grain size in light of the Olson–Cohen theory of heterogeneous martensitic nucleation, and concluded that, in the case of coarse austenite grains, high stress triaxiality promotes both stress-assisted and strain-induced transformation at low strains [16]. It can be inferred that the existence of neighbouring hard particles, such as those in Fig. 11, can reduce the hydrostatic stress in austenite before transformation, which may be one of the reasons why the coarse austenite grains exhibit obvious retardation in transformation.

4.2.3. Dispersion in the data for individual grains

Wide dispersion in the data for individual austenite grains was seen in Figs. 6,8,9, and 10. The austenite-to-martensite transformation is inherently accompanied by volume expansion, which has a significant influence on the transformation behaviour of neighbouring austenite grains. The influence of neighbouring hard phases (here, emerging martensite) has already been discussed. The influence of the austenite grain itself and the surrounding ferrite phase are discussed below.

Fundamentally, in this context, the chemical driving force is a function of the chemical composition of austenite. Of the three constitutive chemical elements of C-Mn-Si multi-phase steel, the diffusion of Mn is relatively slow at an intermediate processing temperature range such as 650 °C. Mn is therefore less apt to distribute homogeneously in C-Mn-Si multi-phase steel, thereby causing spatial variation in austenite stability [15]. According to the nanoindentation experiments performed by He et al., ferrite has only a small variation in hardness, while a large scatter is observed in austenite grains [47]. He et al. attributed the latter to the grain boundary structure of austenite, in addition to the effects of inhomogeneous Mn distribution.

In addition, it is of crucial importance to evaluate the effect of the underlying soft ferrite phase, which was not performed in this study. It has been reported that preferential transformation was observed in the case of austenite grains located at the triple junctions amongst ferrite grains, especially for larger ferrite grains, due to their low stability, in contrast to the austenite grains that were completely embedded in larger ferrite grains [19]. This would be partly attributable to stress localization at the grain boundaries. As noted in SubSection 4.2.1, the underlying ferrite also exerts marked effects on the rotation behaviour of austenite grains. Another point to note is that the true nature of the austenite-to-martensite transformation is also associated with the crystallographic relationship between the transforming martensite and the surrounding ferrite. According to Yamashita et al., austenite grains are prone to transform such that the crystallographic orientation of the consequent martensite variant matches that of the surrounding ferrite matrix [43]. This might function as an additional cause of the dispersion in austenite stability.

5. Conclusion

The gradual transformation behaviour of individual austenite grains, which lasted for more than 8% in applied strain, was clearly observed in 3D. The individual transformation behaviours were classified based on the initial crystallographic orientation and size of the grains. Drastic reduction in the retained austenite volume fraction (i.e., from 22.8 to 6.8% on average) occurred between an applied strain of 0.3 and 3.5%; and coarse austenite grains, which are typically greater than 2.5 μm in diameter, remained until an applied strain of approximately 3 - 6% on average was applied. A number of grains were rotated to a non-negligible extent (e.g., 2.0° on average for an applied strain of 5.8%), and some of the high Schmid factor grains (e.g., those of 0.48 or higher) were rotated instead of being transformed, sometimes resulting in a reduction in the Schmid factor. The retained austenite grains with a tensile axis within 15° of their initial ⟨110⟩ direction exhibited somewhat rapid transformation (i.e., about 38% of the initial volume fraction at an applied strain of 1.3%), whereas those within 15° of the initial ⟨111⟩ direction exhibited a below-average transformation rate transformation (i.e., also about 38% of the initial volume fraction at an applied strain of 3.5%). This was consistent with the measured dislocation multiplication behaviour of the individual grains.

Coarse austenite grains were prone to rapid transformation, which is contrary to what is reported in the literature: the level of external strain at which the coarse austenite grains were fully transformed to martensite was more than double (i.e., 4.7% for grains larger than 2.5 μm in diameter) the corresponding level for fine austenite grains (i.e., 2.0% for grains smaller than 2.5 μm in diameter). This was attributed to the influence of multi-variant martensite transformed from the coarse austenite grains.

During the early loading stages (i.e., an applied strain range of 0 - 0.5%), austenite grains with higher driving forces tended to preferentially commence transformation. The early stage of the transformation was thus associated with the stress-assisted transformation controlled by the mechanical driving force, whilst the overall transformation was interrelated with the strain-induced transformation controlled by the dislocation multiplication. It is also noteworthy that the data for individual austenite grains was widely dispersed, and it was clearly demonstrated that such characteristic behaviour was owing to the grains' interactions with neighbouring phases. For example, the martensite emerging adjacently to austenite inevitably caused retardation in the transformation, along with the gradual dislocation density increase due to strong deformation constraint.

Declaration of Competing Interest

The authors declare that they have no known competing financial interests or personal relationships that could have appeared to influence the work reported in this paper.

Acknowledgements

This work was partly supported by JSPS KAKENHI Grant Numbers JP17H01328 and JP21H04624. HT is grateful to Prof. T. Tsuchiyama of Kyushu University for his valuable advice, and also to Messrs. K. Takeda and K. Ishikawa of Nippon Steel Corporation for experimental supports and discussions. The synchrotron experiments were performed with the approval of JASRI, through proposal numbers 2018A0076, 2018B0076, 2019A0076, and 2019B0076.

Supplementary materials

Supplementary material associated with this article can be found, in the online version, at doi:10.1016/j.actamat.2022.117956.

References

[1] C. Horvath, C.M. Enloe, J. Singh, J. Coryell, Persistent challenges to advanced high strength steel implementation, Iron Steel Technol. 14 (2017) 76–83.
[2] R. Alturk, L.G. Hector Jr, C.M. Enloe, F. Abu-Farha, T.W. Brown, Strain rate effect on tensile flow behavior and anisotropy of a medium manganese TRIP steel, JOM 70 (2018) 894–905.
[3] V. Savic, L.G. Hector, H. Singh, M. Paramasuwom, U. Basu, A. Basudhar, N. Stander, Development of a lightweight third-generation advanced high-strength steel (3GAHSS) vehicle body structure, Soc. Autom. Engineers Int. J. Mater. Manf. 11 (2018) 303–313.
[4] G. Reisner, E.A. Werner, P. Kerschbaummayr, I. Papst, F.D. Fischer, The modeling of retained austenite in low-alloyed TRIP steels, JOM 49 (1997) 62–65.
[5] G.N. Haidemenopoulos, A.N. Vasilakos, Modelling of austenite stability in low-alloy triple-phase steels, Steel Res. 67 (1996) 513–519.

[6] A. Devaraj, Z. Xu, F. Abu-Farha, X. Sun, L.G. Hector, Nanoscale solute partitioning and carbide precipitation in a multiphase TRIP steel analyzed by atom probe tomography, JOM 70 (2018) 1752–1757.
[7] H.W. Luo, J. Shi, C. Wang, X. Sun, H. Dong, Experimental and numerical analysis on formation of stable austenite during the intercritical annealing of 5Mn steel, Acta Mater. 59 (2011) 4002–4014.
[8] J. Han, S.-J. Lee, J.-G. Jung, Y.K. Lee, The effects of the initial martensite microstructure on the microstructure and tensile properties of intercritically annealed Fe–9Mn–0.05C steel, Acta Mater. 78 (2014) 369–377.
[9] O. Matsumura, Y. Sakuma, H. Takechi, Enhancement of elongation by retained austenite in intercritical annealed 0.4C-1.5Si-0.8Mn steel, Trans. ISIJ 21 (1987) 570–579.
[10] C.G. Lee, S.-J. Kim, T.-H. Lee, S. Lee, Effects of volume fraction and stability of retained austenite on formability in a 0.1C–1.5Si–1.5Mn–0.5Cu TRIP-aided cold-rolled steel sheet, Mater. Sci. Engng. A 371 (2004) 16–23.
[11] M.L. Brandt, G.B. Olson, Bainitic stabilization of austenite in low alloy sheet steels, Iron Steelmak. 20 (1993) 50–60.
[12] K. Sugimoto, M. Misu, M. Kobayashi, H. Shirasawa, Effects of second phase morphology on retained austenite morphology and tensile properties in a trip-aided dual-phase steel sheet, ISIJ Int 33 (1993) 775–782.
[13] P.J. Jacques, Q. Furneḿont, F. Lani, T. Pardoen, F. Delannay, Multiscale mechanics of TRIP-assisted multiphase steels, Acta Mater. 55 (2007) 3681–3693.
[14] L. Samek, E. De Moor, J. Penning, B.C. De Cooman, Influence of alloying elements on the kinetics of strain-induced martensitic nucleation in low-alloy, multiphase high-strength steels, Metall. Mater. Tran. A 37 (2006) 109–124.
[15] Z.H. Cai, H. Ding, R.D.K. Misra, Z.Y. Ying, Austenite stability and deformation behaviour in a cold-rolled transformation-induced plasticity steel with medium manganese content, Acta Mater. 84 (2015) 229–236.
[16] G.N. Haidemenopoulos, N. Aravas, I. Bellas, Kinetics of strain-induced transformation of dispersed austenite in low-alloy TRIP steels, Mater. Sci. Engng. A 615 (2014) 416–423.
[17] I.B. Timokhina, P.D. Hodgson, E.V. Pereloma, Effect of microstructure on the stability of retained austenite in transformation-induced-plasticity steels, Metall. Mater. Trans. A 35A (2004) 2331–2341.
[18] S. Zhang, K.O. Findley, Quantitative assessment of the effects of microstructure on the stability of retained austenite in TRIP steels, Acta Mater. 61 (2013) 1895–1903.
[19] G.K. Tirumalasetty, M.A. van Huis, C. Kwakernaak, J. Sietsma, W.G. Sloof, H.W. Zandbergen, Deformation-induced austenite grain rotation and transformation in TRIP-assisted steel, Acta Mater. 60 (2012) 1311–1321.
[20] J. Chiang, B. Lawrence, D. Boyd, A.K. Pilkey, Effect of microstructure on retained austenite stability and work hardening of TRIP steel, Mater. Sci. Engng. A 528 (2011) 4516–4521.
[21] O. Murańsky, P. S¨ittner, J. Zrnı́k, E.C. Oliver, In situ neutron diffraction investigation of the collaborative deformation–transformation mechanism in TRIP-assisted steels at room and elevated temperatures, Acta Mater. 56 (2008) 3367–3379.
[22] M.R. Berrahmoune, S. Berveiller, K. Inal, A. Moulin, E. Patoor, Analysis of the martensitic transformation at various scales in TRIP steel, Mater. Sci. Engng. A 378 (2004) 304–307.
[23] C.P. Scott, J. Drillet, A study of the carbon distribution in retained austenite, Scripta Mater 56 (2007) 489–492.
[24] S.Y.P. Allain, S. Gaudez, G. Geandier, J.-C. Hell, M. Gouné, F. Danoix, M. Soler, S. Aoued, A. Poulon-Quintin, Internal stresses and carbon enrichment in austenite of quenching and partitioning steels from high energy X-ray diffraction experiments, Mater. Sci. Engng. A 710 (2018) 245–250.
[25] K.S. Choi, W.N. Liu, X. Sun, M.A. Khaleel, Y. Ren, Y.D. Wang, Advanced micromechanical model for transformation-induced plasticity steels with application of in-situ high-energy x-ray diffraction method, Metall. Mater. Trans. A 39A (2008) 3089–3096.
[26] H.F. Poulsen, Three-Dimensional X-Ray Diffraction Microscopy, Mapping Polycrystals and Their Dynamics (Springer Tracts in Modern Physics), Springer, Berlin, 2004.
[27] H. Toda, T. Kamiko, Y. Tanabe, M. Kobayashi, D.J. Leclere, K. Uesugi, A. Takeuchi, K. Hirayama, Diffraction-amalgamated grain boundary tracking for mapping 3D crystallographic orientation and strain fields during plastic deformation, Acta Mater. 107 (2016) 310–324.
[28] N.H.van Dijk Jimenez-Melero, L. Zhao, J. Sietsma, S.E. Offerman, J.P. Wright, S. van der Zwaag, Martensitic transformation of individual grains in low-alloyed TRIP steels, Scripta Mater. 56 (2007) 421–424.
[29] H. Toda, Y. Ohkawa, T. Kamiko, T. Naganuma, K. Uesugi, A. Takeuchi, Y. Suzuki, M. Kobayashi, Grain boundary tracking: a four-dimensional visualization technique for determining grain boundary geometry via local strain mapping, Acta Mater. 61 (2013) 5535–5548.
[30] H. Toda, A. Takijiri, M. Azuma, S. Yabu, K. Hayashi, D. Seo, M. Kobayashi, K. Hirayama, A. Takeuchi, K. Uesugi, Damage micromechanisms in dual-phase steel investigated with combined phase- and absorption-contrast tomography, Acta Mater. 126 (2017) 401–412.
[31] A. Takeuchi, K. Uesugi, M. Uesugi, H. Toda, K. Hirayama, K. Shimizu, K. Matsuo, T. Nakamura, High-energy x-ray nanotomography introducing an apodization Fresnel zone plate objective lens, Rev. Sci. Instrum. 92 (2021) 023701.
[32] A.N. Vasiliakos, K. Papamantellos, G.N. Haidemenopoulos, W. Bleck, Experimental determination of the stability of retained austenite in low alloy TRIP steels, Steel Res. 70 (1999) 466–471.
[33] H. Toda, C.T. X-Ray, Hardware and Software Techniques, 2021 Springer Nature Singapore.
[34] D. Bradley, G. Roth, Adaptive thresholding using the integral image, J. Graphics Tools 12 (2007) 13–21.
[35] T. Ungár, S. Ott, P.G. Sanders, A. Borbély, J.R. Weertman, Dislocations, grain size and planar faults in nanostructured copper determined by high resolution X-ray diffraction and a new procedure of peak profile analysis, Acta Mater. 46 (1998) 3693–3699.
[36] F. Abu-Farha, X. Hu, X. Sun, Y. Ren, L.G. Hector Jr, G. Thomas, T.W. Brown, In situ local measurement of austenite mechanical stability and transformation behavior in third-generation advanced high-strength steels, Metall. Mater. Tran. A 49 (2018) 2583–2596.
[37] J.R. Patel, M. Cohen, Criterion for the action of applied stress in the martensitic transformation, Acta Metall. 1 (1953) 531–536.
[38] H.K.D.H. Bhadeshia, R.W.K. Honeycombe, Steels – Microstructure and Properties, 3rd ed., Elsevier, Oxford, UK, 2006.
[39] T. Hayashi, S. Morito, T. Ohba, Lath and butterfly composite martensite microstructure of a medium-carbon steel and its quantitative evaluation, ISIJ Int. 58 (2018) 1524–1531.
[40] N. Tsuchida, T. Tanaka, Y. Toji, Analysis of tensile deformation behaviour by in situ neutron diffraction experiments, Tetsu-to-Hagane 105 (2019) 918–926.
[41] F. Lani, Q. Furneḿont, T. Van Rompaey, F. Delannay, P.J. Jacques, T. Pardoen, Multiscale mechanics of TRIP-assisted multiphase steels: II. Micromechanical modelling, Acta Mater. 55 (2007) 3695–3705.
[42] G.N. Haidemenopoulos, M. Grujicic, G.B. Olson, M. Cohen, Thermodynamics-based alloy design criteria stabilization and transformation toughening in system, J. Alloys Compd. 220 (1995) 142–147.
[43] T. Yamashita, N. Koga, O. Umezawa, Martensitic transformation of retained austenite in ferrite matrix for low alloy steel, Mater. Trans. 59 (2018) 712–716.
[44] P. Hou, Y. Li, D. Chae, Y. Ren, K. An, H. Choo, Lean duplex trip steel: role of ferrite in the texture development, plastic anisotropy, martensitic transformation kinetics, and stress partitioning, Materialia 15 (2021) 100952.
[45] S. Takaki, K. Fukunaga, J. Syarif, T. Tsuchiyama, Effect of grain refinement on thermal stability of metastable austenitic steel, Mater. Trans. 45 (2004) 2245–2251.
[46] G. Miyamoto, N. Iwata, N. Takayama, T. Furuhara, Quantitative analysis of variant selection in ausformed lath martensite, Acta Mater. 60 (2012) 1139–1148.
[47] B.B. He, M.X. Huang, Z.Y. Liang, A.H.W. Ngan, H.W. Luo, J. Shi, W.Q. Cao, H. Dong, Nanoindentation investigation on the mechanical stability of individual austenite grains in a medium-Mn transformation-induced plasticity steel, Scripta Mater. 69 (2013) 215–218.